Bound states in the continuum and Fano resonances in photonic and plasmonic loop structures

Madiha Amrani, Soufyane Khattou, Housni Al-Wahsh, Yamina Rezzouk, El Houssaine El Boudouti, Cécile Ghouila-Houri, Abdelkrim Talbi, Abdellatif Akjouj, L. Dobrzynski, Bahram Djafari-Rouhani

Bound states in the continuum and Fano resonances in photonic and plasmonic loop structures

Madiha Amrani[1], Soufyane Khattou[1], Housni Al-Wahsh[2], Yamina Rezzouk[1], El Houssaine El Boudouti[1], Cecile Ghouila-Houri[3], Abdelkrim Talbi[3], Abdellatif Akjouj[4], Leonard Dobrzynski[4], Bahram Djafari-Rouhani[4]

[1] LPMR, Département de Physique, Faculté des Sciences, Université Mohammed I, Oujda, Morocco

[2] Engineering Mathematics and Physics Department, Faculty of Engineering, Benha University, Cairo, Egypt

[3] Univ. Lille, CNRS, Centrale Lille, ISEN, Univ. Valenciennes, UMR 8520 -IEMN - LIA LICS/LEMAC, F-59000 Lille, France

[4] Département de Physique, IEMN, UMR CNRS 8520, Université de Lille, 59655 Villeneuve d'Ascq, France

Abstract

The design and study of structures exhibiting bound states in the continuum (BICs) are the object of continuous works in wave physics. These long-lived states which are localized in some parts of the system without interacting with the background have found several potential applications due to their high sensitivities to weak perturbations, in particular in filtering and sensing. In this paper, we present a theoretical demonstration of BICs in an asymmetric loop composed of two arms of lengths d_1 and d_2 with both an experimental validation in the radio-frequency (RF) domain using coaxial cables and a numerical validation in the infrared (IR) domain using plasmonic metal-insulator-metal nanometric waveguides. The analytical study is performed by means of the Green's function method, whereas the numerical calculation is obtained using finite element method. The BICs correspond to localized resonances of infinite lifetime inside the loop, without any leakage into the surrounding waveguides. We demonstrate that the condition for the existence of the BICs is to make the lengths of the two arms (d_1 and d_2) commensurate with each other. At the corresponding frequencies, one of the two degenerate modes of the isolated loop (associated with the clockwise and anti-clockwise propagations) couples to the waveguides while the other remains unaffected. When the lengths are slightly shifted from the BICs, the latter transform to Fano resonances exhibiting dips in the transmission spectra and sharp peaks in the density of states (DOS). As an application of our design, we show the efficiency of the Fano resonances in designing an efficient gaz-sensor with a high sensitivity and factor of merit in the IR domain. In addition, we derive an exact formula about the proportionality between DOS and the derivative of the argument of the determinant of the scattering matrix (Friedel phase) for a lossless structure; then, we discuss the validity and deviation from this rule when the loss is increased.

✉ El Houssaine El Boudouti
elboudouti@yahoo.fr

1 Introduction

Bound states in the continuum (BICs) have brought significant attention over the last decades due to their important design principle to create systems with infinite quality factors in order to enhance light-matter interaction (Hsu et al. 2016). BICs, also known as trapped modes, manifest as resonances with zero linewidths in lossless systems. In other words, they reside inside the continuous spectrum of extended states but remain perfectly confined in some parts of the system. The concept of BICs was first predicted in quantum mechanics by Von Neumann and Wigner (1929) in 1929. Since then, BICs were found in various fields of physics such as photonics (Bogdanov et al. 2019; He et al. 2021), acoustics (Huang et al. 2021; Amrani et al. 2021; Quotane et al. 2018), mesoscopics (Mrabti et al. 2020; Bulgakov et al. 2006) and plasmonics (Sun et al. 2021; Qi et al. 2021; Xie et al. 2020). Thanks to their high quality factors, they are very promising for many applications such as lasers (Ha et al. 2018), filters (Doskolovich et al. 2019; Cui et al. 2016) and sensors (Wu et al. 2019; Conteduca et al. 2021). BICs can be categorized into several mechanisms based on their physical origin (Hsu et al. 2016). Among them, one can cite, symmetry-protected BICs, Fabry-Perot (FP) BICs and Freidrich-Wintgen BICs which have been subsequently investigated theoretically and experimentally in different physical systems (Amrani et al. 2021; Zhao et al. 2020; Algorri et al. 2021; Azzam et al. 2018; Pankin et al. 2020). These modes are not observable from the continuous spectrum due to their non-radiative property with vanishing spectral linewidth. However, they can exist only under an appropriate choice of the geometrical or material parameters of the system and/or under specific external perturbations. Thus, by slightly detuning the system from the BIC conditions (for example, changing the geometrical parameters), the latter transforms to a quasi-BIC with a finite width. Generally, the quasi-BIC manifests itself as a Fano resonance when it falls in the vicinity of a zero of transmission. Let us recall that the Fano resonance is characterized by a resonance followed by an antiresonance over a narrow frequency range giving rise to an asymmetrical line profile (Fano 1961). This resonance can be explained as the product of two processes of constructive and destructive interferences between a discrete state and a continuum background (Fano 1961; Miroshnichenko et al. 2010).

Loop structures made of two arms are an excellent platform to explore BICs as well as Fano effects. For instance, Fano resonances have been studied in a mesoscopic loop with and without a quantum dot in one arm. The loop is placed under the action of a magnetic flux called Aharonov-Bohm (A-B) effect (Wu et al. 2008; Kobayashi et al. 2004; Xiong and Liang 2004). Also, giant persistent currents and Fano resonances have been studied in single and double asymmetric rings with and without scatterers on both arms or in presence of stubs around the loop (Hsueh et al. 2013; Mrabti et al. 2018; Voo and Chu 2005; Al-Wahsh et al. 2007). Fano resonances have been obtained by tailoring the lengths of the wires constituting the system or the magnetic flux through the loop (Bulgakov et al. 2006; Voo and Chu 2005; Al-Wahsh et al. 2007). In plasmonic systems, different ring resonators based on metal-insulator-metal (MIM) structures and side branches attached to waveguides, have been proposed to study Fano resonances and for sensing applications (Chou Chao et al. 2021; Rakhshani 2019; Chen et al. 2021; Hajshahvaladi et al. 2022; Liu et al. 2021). In photonic systems, little works have been devoted to study BICs and Fano resonances in loop structures placed between two waveguides. For example, El Boudouti et al. (2004) have studied the possibility to realize superluminal phenomenon in an asymmetric loop structures as a consequence of the destructive interference between the waves in the two arms of the loop like in Mach-Zehnder interferometers (Sánchez-Meroño et al. 2014;

Zou et al. 2015). The same structure has been studied in acoustic tubes (Robertson et al. 2007). However, to our knowledge, an analytical and experimental study of BICs and Fano resonances in a single asymmetric photonic loop structure, has not been treated before.

In this paper, we consider a simple photonic loop which is a good candidate to obtain BICs and Fano resonances. The loop is composed of two connected wires of lengths d_1 and d_2. The length of the loop $L = d_1 + d_2$ is considered fix, whereas the detuning between the two wires $\delta = d_2 - d_1$ is taken variable (Fig. 1). The asymmetric loop is placed between two semi-infinite leads (Fig. 1). Using the Green's function method (Dobrzynski et al. 2020), we give a clear analytical demonstration of BICs in a loop under specific values of the detuning δ with an experimental confirmation in the radio-frequency performed with coaxial cables and a numerical validation in the infrared region based on finite element method (FEM) using Comsol Multiphysics. We demonstrate that the BICs only appear when the two arms of the loop are taken commensurate (i.e., $\frac{d_2}{d_1} = \frac{n}{m}$ where m and n are non-zero integers) in such a way that the electric field vanishes at the connecting points with the semi-infinite wires, leading to uncoupled stationary modes in the loop within the continuum states of the waveguide. These modes represent FP-type BICs (Hsu et al. 2016; Sadreev 2021). By slightly shifting δ from BIC conditions, the FP-BICs collapse to specific Fano resonances with finite lifetime known as quasi-BICs with an anti-resonance shape. In addition, by taking into account the loss in the loop structure, we show that there exists a threshold value of δ where the absorption tends to a maximum value, this happens when the transmission and reflection coefficients become equal (around 22 %). Also, we provide a comparison between the density of states (DOS) of the system which is a fundamental physical quantity and the derivative of the phase of the determinant of the scattering matrix, the so-called Friedel phase (Friedel 1952) which is measurable in the transmission experiment. In particular, we show the similarities and differences between these two quantities as function of δ. Finally, considering plasmonic MIM waveguides and loop of nanometric size, we confirm our analytical results by FEM simulations of the plasmonic structure in the infrared domain and highlight the efficiency of the proposed design for gas sensing applications.

The rest of the paper is organized as follows: In Sect. 2, we give a brief review of the method of calculation based on the Green's function approach. We provide an analytical expression of the dispersion relation of BICs and a relationship between the DOS and the derivative of the Friedel phase. Section 3 is devoted to the analytical and experimental results in the radio-frequency, whereas section 4 provides numerical results of the plasmonic MIM structure in the infrared region. The conclusions are presented in Sect. 5.

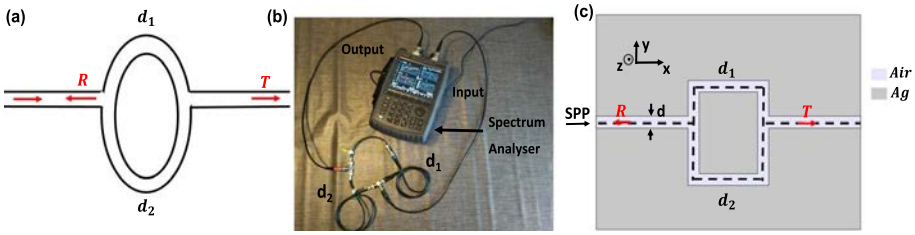

Fig. 1 **a** Schematic representation of the asymmetric loop with different lengths d_1 and d_2 inserted between two semi-infinite leads. **b** Experimental setup for the study of the loop system performed with standard coaxial cables and a network vectorial analyzer. The lengths are indicated in accordance with (a). **c** Schematic representation of the plasmonic nanowaveguide loop used in Comsol simulation

2 Theoretical Results

2.1 Theoretical model: Green's function elements

We consider an infinite homogeneous isotropic dielectric wire characterized by its impedance Z and the relative permittivity ε. An electromagnetic wave field is propagating through the cable in the dielectric-field space between the center conductor and shield. In the limit where the widths of the wires are much smaller than their lengths, the telegrapher's equation describing microwave networks, the so-called TEM waves, is given by Dobrzynski et al. (2020)

$$\left[\frac{\partial^2}{\partial x^2} + \frac{\omega^2\varepsilon}{c^2}\right] E(x) = 0 \tag{1}$$

where c is the speed of light in vacuum, and ω is the angular frequency of the wave. Then, the corresponding Green's function between two points x and x' of this wire is defined by

$$\left[\frac{\partial^2}{\partial x^2} + \frac{\omega^2\varepsilon}{c^2}\right] G(x, x') = \delta(x - x') \tag{2}$$

The solution of Eq. (2) is given by Dobrzynski et al. (2020)

$$G(x, x') = -j\frac{e^{-jk|x-x'|}}{2F}, \tag{3}$$

where $F = \frac{\omega}{Z}$, $k = \omega\sqrt{\varepsilon}/c$, and $j = \sqrt{-1}$. Let us recall that $\sqrt{\varepsilon} = n$ defines the index of refraction of the coaxial. Its inverse called the velocity factor is given by $V_F = \frac{1}{c\sqrt{LC}}$ where L and C are the inductance and the capacitance per unit length of the cable, respectively. L and C are frequency dependent. As mentioned above, the validity of our results is subject to the requirement that the cross section of the waveguide is negligible compared to their length and to the propagation wavelength, then the assumption of mono-mode waveguide is satisfied.

Before giving the theoretical results of the transmission and reflection coefficients as well as the dispersion relation and DOS, we will recall briefly the expression of the Green's function of the different wires from which the loop system is composed, namely:

(i) The inverse of the Green's function $g_i^{-1}(M_iM_i)$ of a finite segment of length d_i in the space of its interface $M_i = \{0, d_i\}$ can be written as a (2×2) matrix (Dobrzynski et al. 2020)

$$g_i^{-1}(M_iM_i) = \begin{pmatrix} -\frac{FC_i}{S_i} & \frac{F}{S_i} \\ \frac{F}{S_i} & -\frac{FC_i}{S_i} \end{pmatrix}, \tag{4}$$

where $C_i = \cos(kd_i)$, $S_i = \sin(kd_i)$, $F = \frac{\omega}{Z}$, and $k = \frac{\omega\sqrt{\varepsilon}}{c}$ $(i = 1, 2)$. It should be noted that these and the following expressions remain valid even for a dispersive material (such as in plasmonics) where the permittivity ε is a function of ω.

(ii) The inverse of the Green's function $g_0^{-1}(MM)$ in the space of interfaces $M = \{1, 2\}$ (Fig. 1) of an asymmetric loop is given by the superposition of two (2×2) matrices given in Eq. (4) (Dobrzynski et al. 2020) for each wire i

$$g_0^{-1}(MM) = \begin{pmatrix} a & b \\ b & a \end{pmatrix}, \tag{5}$$

where $a = -F(\frac{C_1}{S_1} + \frac{C_2}{S_2})$ and $b = F(\frac{1}{S_1} + \frac{1}{S_2})$.

(iii) The inverse of the Green's function of a semi-infinite wire is given by Dobrzynski et al. (2020)

$$g_s^{-1}(i,i) = -jF, \tag{6}$$

where $j = \sqrt{-1}$.

2.2 Transmission and reflection coefficients and conditions for BICs

The photonic structure presented in Fig. 1a is composed by an asymmetric loop made of two wires of lengths d_1 and d_2. The system is inserted between two semi-infinite wires. The inverse of Green's function of the whole photonic system is given by a linear superposition of the Green's functions of its constituents given above (Eqs. (5) and (6)) in the interface space $M = \{1, 2\}$ leading to a (2×2) matrix, namely (Dobrzynski et al. 2020)

$$g^{-1}(MM) = \begin{pmatrix} a - jF & b \\ b & a - jF \end{pmatrix}. \tag{7}$$

Let us consider an incident wave $U(x) = e^{-jkx}$ launched in the left semi-infinite wire (Fig. 1). From Eq. (7), one can obtain the transmission coefficient in the right semi-infinite wire, namely, $t = -2jFg(1,2)$, or equivalently

$$t = \frac{4\sin(kL/2)\cos(k\delta/2)}{5\sin^2(kL/2) - \sin^2(k\delta/2) + j4\sin(kL/2)\cos(kL/2)}. \tag{8}$$

In the same way, the reflection coefficient in the left semi-infinite wire is given by $r = -1 + 2jFg(1,1)$, or equivalently

$$r = -\frac{5\sin^2(kL/2) + \sin^2(k\delta)}{5\sin^2(kL/2) - \sin^2(k\delta/2) + j4\sin(kL/2)\cos(kL/2)}, \tag{9}$$

where $L = d_2 + d_1$ and $\delta = d_2 - d_1$.

From the expressions of t (Eq. (8)) and r (Eq. (9)), one can deduce the transmission and reflection rates as $T = |t|^2$ and $R = |r|^2$. Therefore, in the absence of loss (i.e., k is real), one can check easily the conservation law $R + T = 1$. However, in presence of loss, (i.e., k is complex) the absorption coefficient can be obtained from the equation $A = 1 - R - T$.

It is well known that the eigenmodes of the system are given by the poles of the transmission coefficient t (Eq. (8)) or equivalently by the poles of the Green's function (Eq. (7)), namely

$$5\sin^2(kL/2) - \sin^2(k\delta/2) + j4\sin(kL/2)\cos(kL/2) = 0. \tag{10}$$

This latter equation is a complex quantity. Its real part gives the position of the resonances in transmission and DOS, whereas its imaginary part is related to the width of the resonance. In general, it is not easy to simultaneously cancel the real and imaginary parts of Eq.(10) at the same frequency. This will correspond to a bound state falling in the

continuum of states. In order to avoid the divergence of t, then its numerator should also vanish in such a way that t becomes finite. These two conditions can be fulfilled only if $\sin(\frac{kL}{2}) = 0$ and $\sin(\frac{k\delta}{2}) = 0$. Therefore, we get the following condition

$$\frac{d_1}{d_2} = \frac{m}{n}, \tag{11}$$

where m and n are two odd or two even integers (i.e., $m + n = 2p$). This means that the lengths d_1 and d_2 should be commensurate with each other. To give a physical picture of the BICs situation, we have defined a unit length d_0 such that the lengths in the two arms of the loop are multiple of d_0 ($d_1 = md_0$ and $d_2 = nd_0$). Now, the lowest (fundamental) BIC frequency f_0 will be defined such that the unit length d_0 accommodates half of the corresponding wavelength ($\lambda_0 = 2\pi/k = (2\pi\sqrt{\varepsilon}c)/f_0$). Then, the number of wavelengths in the whole loop will be an integer multiple of λ_0 ($(m + n)\lambda_0/2 = p\lambda_0$), but this number can be divided among the two arms as integer or half-integer numbers of λ_0. The higher (excited) BIC frequencies are the multiple of f_0. Also, notice that the eigenfunction of the BIC will have zero amplitude at the junction points with the semi-infinite waveguides.

To express the conclusion differently, let us note that Eq. (10) can be written explicitly as

$$\sin(kd_0)\left\{5\sin(kd_0)U^2_{n+m}(S_0) - \sin(kd_0)U^2_{n-m}(S_0) + j8U_{n+m}(S_0)\cos[kd_0(m+n)/2]\right\} = 0, \tag{12}$$

where $U_{n+m}(S_0)$ and $U_{n-m}(S_0)$ represent Chebyshev Polynomials of the Second kind and $S_0 = \sin(kd_0/2)$.

Therefore, the BICs are given by $sin(kd_0) = 0$. These modes occur for

$$\delta = 2\left(\frac{m-n}{m+n}\right)\frac{L}{2} \text{ and } \frac{kL}{2\pi} = \frac{m+n}{2} = p. \tag{13}$$

Also, we can show easily that the transmission T reaches unity at the BIC condition. Let us mention that the single loop without the semi-infinite wires exhibits two degenerate modes given by $\sin(kL/2) = 0$ (or $\sin(kd_0/2) = 0$). Now, in presence of the semi-infinite wires, Eq. (12) shows that one of the two modes remains a BIC, whereas the second mode interacts strongly with the continuum states of the surrounding media (see below).

2.3 Density of states and Friedel phase

Another interesting quantity that can be deduced from the Green's function is the density of states (DOS). In order to provide an analytical comparison of the DOS with the phases involved in the scattering matrix, we consider the variation of DOS ($\Delta n(\omega)$) between the loop system depicted in Fig. 1 and a reference system formed out of the same volumes of the decoupled semi-infinite wires and the isolated loop. This quantity is given by

$$\Delta n(\omega) = \frac{-1}{\pi}\frac{d}{d\omega}Arg\left\{det\left[\frac{g(M,M)}{g_0(M,M)F^2}\right]\right\}. \tag{14}$$

For a lossless system, the expression of $det[g(M, M)]$ can be derived from the matrix in Eq. (7) as follows

$$det[g(M,M)] = -\frac{S_1 S_2}{F^2\{5\sin^2(kL/2) - \sin^2(k\delta/2) + j4\sin(kL/2)\cos(kL/2)\}}. \quad (15)$$

Also, the expression of $det[g_0(M,M)]$ is obtained from the matrix in Eq. (5), namely

$$det[g_0(M,M)] = -\frac{S_1 S_2}{4F^2\sin^2(kL/2)}. \quad (16)$$

Now, if we do not take into account the discrete eigenmodes of the isolated loop system (i.e, $\sin(kL/2) = 0$), then Eq. (14) becomes simply

$$\Delta n(\omega) = -\frac{1}{\pi}\frac{d}{d\omega}\arctan\left\{\frac{4\sin(kL/2)\cos(kL/2)}{5\sin^2(kL/2) - \sin^2(k\delta/2)}\right\}. \quad (17)$$

It is worth noticing that a slightly different expression of the variation of DOS ($\Delta n'(\omega)$) can be obtained by considering the difference between the structure in Fig. 1 and a reference system made of the infinite wire. This quantity can be derived by integrating the local DOS over the whole structure and subtracting the DOS of the infinite wire.

In addition to the information that can be deduced from the transmission and reflection coefficients, other supplementary informations can be deduced from the modulus and argument of the determinant of the scattering matrix defined as

$$S = \begin{pmatrix} r & t \\ t & r \end{pmatrix} \quad (18)$$

where t and r are the transmission and reflection coefficients given by Eqs. (8) and (9) respectively.

Indeed, we provide an analytical comparison between the scattering Friedel phase defined as Friedel (1952) $\theta_f = Arg[det(S)]$ and $\Delta n(\omega)$. The determinant of the scattering matrix S (Eq. (18)) for the loop system is given by

$$det(S) = r^2 - t^2 = \frac{[3\sin^2(kL/2) + \sin^2(k\delta/2)]^2 + [4\sin(kL/2)\cos(kL/2)]^2}{\left[5\sin^2(kL/2) - \sin^2(k\delta/2) + j4\sin(kL/2)\cos(kL/2)\right]^2}. \quad (19)$$

For the lossless system, one can show easily the well known relation satisfied by $det(S)$ (i.e., $|det(S)| = 1$) and

$$\theta_f = Arg[det(S)] = -2\arctan\left\{\frac{4\sin(kL/2)\cos(kL/2)}{5\sin^2(kL/2) - \sin^2(k\delta/2)}\right\}. \quad (20)$$

Hence, one can deduce from Eqs. (17) and (20) that

$$\frac{d\theta_f}{d\omega} = 2\pi\Delta n(\omega). \quad (21)$$

However, for a lossy system, the analytical equation (21) is no longer valid. We will provide numerically and experimentally the effect of the presence of loss on the above results. In particular, we show that the absorption A can be also extracted from $|det(S)|$ through the relation $|det(S)| \simeq 1 - A$, also A reaches a maximum value of 0.55 for a threshold value of δ_{th} around the BIC where $R = T \simeq 0.22$. In addition, we show that $\frac{d\theta_f}{d\omega}$ can exhibit a different behavior in comparison with DOS depending on whether $\delta < \delta_{th}$ or $\delta > \delta_{th}$ (see below).

It is worth noting that Eq. (21) has been obtained in mesoscopic systems in absence of loss (Büttiker 1993; Lee 1999), however, there are little works on such relationship in presence of loss (Khattou et al. 2020).

3 Analytical and experimental results in the radio-frequency domain

In what follows, we will illustrate the theoretical results discussed in Sect. II by presenting numerical and experimental results along the following lines. As mentioned previously, the loop structure can exhibit BICs and Fano resonances. BICs are described as resonances with zero widths in the transmission and DOS spectra. These states can occur only under specific geometrical lengths of the two arms of the loop (i.e., d_1 and d_2 should be commensurate). When departing slightly from the BIC conditions, they transform to specific Fano or EIT resonances that are characterized by a zero Fano parameter q (i.e., $q = 0$). In addition, for lossless systems we show that, if the BIC condition is strictly satisfied the transmission T becomes unity. This kind of BICs represents what we called Fabry-Pérot (FP) BICs as they correspond to stationary modes in the two arms of the loop. For lossy system, we show that the absorption A can reach a maximum value when T and R become equal. The experiments are carried out using coaxial cables in the radio frequency regime. Indeed, we suppose that all wires are standard coaxial cables with the same characteristic impedance $Z \simeq 50\Omega$ and permittivity $\varepsilon = 2.3$. Figure 1b provides a photography of the experimental setup. The details of the experimental procedure can be found in Ref Khattou et al. (2020). In the calculation, the loss is introduced by adding a complex dielectric constant ($\varepsilon = \varepsilon' + j\varepsilon''$) to match the experimental data. The attenuation coefficient α'' can be expressed as $\alpha'' = \frac{\varepsilon'' \omega}{c\sqrt{\varepsilon'}}$.

Figures 2a and b give, respectively, the theoretical variation of the transmission amplitude and DOS (with color scale) versus the dimensionless frequency $\Omega = kL/2\pi$ and the detuning $\delta = d_2 - d_1$ with $L = d_1 + d_2 = 2$ m. The white dots represent the positions of BICs which are solutions of Eq. (13) and for different pairs (m, n) where m and n are of the same parity. One can observe that for each pair (m, n), BICs occur for $\Omega = \frac{m+n}{2} = 1$,

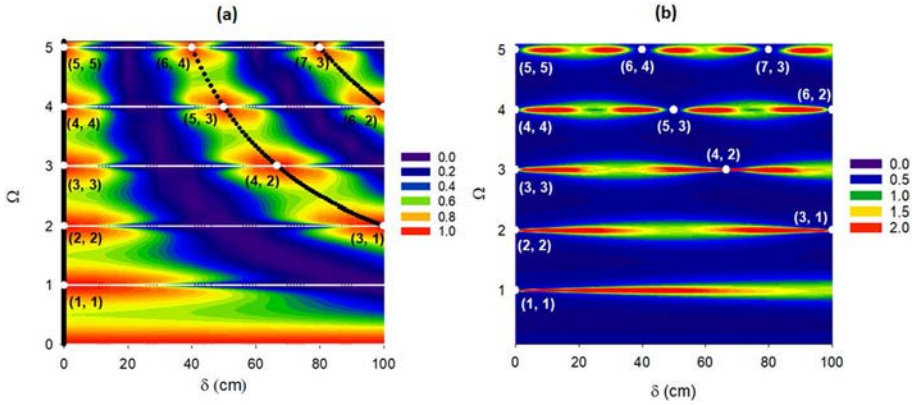

Fig. 2 Variation of transmission (**a**) and DOS (**b**) (with color scale) versus the dimensionless frequency Ω and δ. The white circles indicate the positions of the BICs with different pairs (m, n). The black heavy curves and the white dashed lines in (**a**) represent the modes given by $\sin(k\delta/2) = 0$ and $\sin(kL/2) = 0$, respectively

2,... (i.e., $f = 98$ MHz, 196 MHz,...). These modes appear as the intersection of the curves given by $\sin(kL/2) = 0$ (white dashed lines) and $\sin(k\delta/2) = 0$ (black dotted lines) in Fig. 2a. For any given value of the dimensionless frequency $\Omega = p$ and for δ lying between two BICs, one can notice the shrinking of the dips in the transmission spectra (Fig. 2a) given rise to a full transmission at the BICs; similarly the width of the resonances in the DOS become narrow giving rise to delta peaks at the BICs.

These results confirm the analytical results found in Sect. 2.2. The first BIC falls at $\Omega = 1$ and $\delta = 0$ for the pair $(m = 1, n = 1)$. In the vicinity of this particular point, BIC transforms to a quasi-BIC with a finite lifetime. Generally, the quasi-BIC manifests itself as a Fano resonance in the transmission and a narrow resonance in the DOS. In what follows, we will focus on the BIC associated to the pair $(m = 1, n = 1)$ at $\Omega = 1$ and around $\delta = 0$.

In order to give a better insight about the behavior of the BICs and the associated Fano resonances in the transmission amplitude, we plot in Fig. 3 the transmission and DOS versus the dimensionless frequency Ω for $\delta = 0$ and $\delta = 10$ cm. For $\delta = 0$ (Fig. 3a), the transmission coefficient shows ordinary Fabry-Pérot oscillations. The arrows indicate the positions of the BICs around $\Omega = 1, 2, 3$ where $T = 1$. These modes are hidden and do not give any signature in the transmission spectra because the corresponding resonances have zero width. When we slightly shift the lengths of the two wires (i.e., $\delta \simeq 0$), the BICs induce Fano resonances as shown in Fig. 3c for $\delta = 10$ cm. This result is also clearly visible in the DOS spectra where we can notice for $\delta = 0$ (Fig. 3b) a superposition of F-P broaden resonances and BICs (with infinite lifetime) indicated by vertical lines (delta peaks). For $\delta = 10$ cm (Fig. 3d), the BICs become narrow resonances or quasi-BICs (with a finite lifetime), whereas the broad resonances remain of F-P type. The resonance in Fig. 3c is of Fano shape. Indeed, a Taylor expansion of the transmission amplitude (Eq. (8)) around the resonance at $\Omega = 1$ (i.e., $\Omega = 1 + \epsilon$ with $\epsilon << 1$) enables us to write T following the Fano-shape, namely

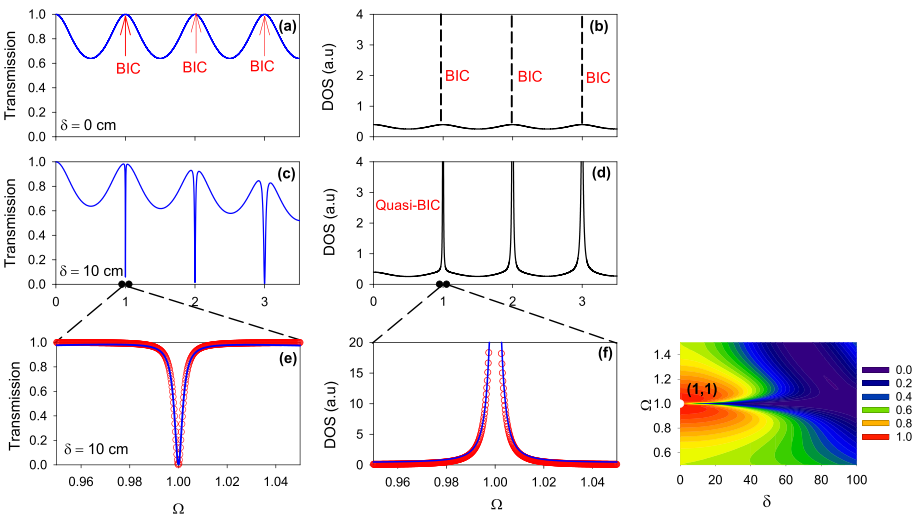

Fig. 3 Transmission and DOS versus the dimensionless frequency $\Omega = kL/2\pi$ for a loop with $\delta = 0$ (**a**), (**b**) and $\delta = 10$ cm (**c**), (**d**). (**e**) and (**f**) Comparison of the approximate results obtained by the Taylor expansion of the transmission and DOS (open circles) around the resonance with the exact calculations (solid lines). The inset shows a zoom of the transmission with color scale around the mode (1, 1) at $\Omega = 1$

$$T = \frac{(\epsilon + q\Gamma/2)^2}{\epsilon^2 + (\Gamma/2)^2}, \tag{22}$$

where $\Gamma = \frac{2(\pi\delta/L)^4}{16+6\pi^2(\delta/L)^4-10\pi^2(\delta/L)^2}$ is the full width at half maximum of the resonance. This is a specific Fano resonance where the Fano parameter $q = 0$ Miroshnichenko et al. (2010); it appears as an anti-resonance in the transmission spectrum (Fig. 3c). Also, by detuning δ this resonance is quantified as electromagnetic induced transparency (EIT) resonance (Limonov et al. 2017). Indeed, the system behaving as an opaque system for $\delta \simeq 0$ around $\Omega = p$ (Fig. 3c) becomes transparent at $\delta = 0$ (Fig. 3a).

In Fig. 3e, we can notice a very good agreement between the exact results of the transmission coefficient (blue line) and the approximate result (red circles) obtained from Eq.(22) around $\Omega = 1$. Also, a Taylor expansion of the $\Delta n(\omega)$ (Eq.(17)) around the resonance at $\Omega = 1$ can be written as

$$\Delta n(\omega) = \frac{B}{\epsilon^2 + (\Gamma/2)^2}, \tag{23}$$

where $B = \frac{(\pi\delta/L)^2}{16+6\pi^2(\delta/L)^4-10\pi^2(\delta/L)^2}$. The results of the approximate expression (Eq. (23)) are shown in Fig. 3f by open circles. These results are in accordance with the exact ones (solid lines).

From Eq. (22) and Figs. 3a and c one can see that for $\delta = 0$, $T = 1$ while for $\delta \neq 0$, $T = 0$ at $\Omega = 1$ (i.e., $\varepsilon = 0$). Similarly, Eq. (23) and Fig. 3b and d show that for $\delta = 0$, $\Delta n(\omega) \to \infty$ and for $\delta \neq 0$, $\Delta n(\omega)$ becomes finite ($\Delta n(\omega)=\frac{4B}{\Gamma^2}$) at $\Omega = 1$.

Now, we discuss the behavior of the transmission spectra when the dissipation in the wires constituting the loop is taken into consideration. Figure 4 provides the transmission and reflection amplitudes as well as the absorption versus the dimensionless frequency Ω for different values of δ. The arrow in Fig. 4a indicates the position of the BIC. The blue lines correspond to the theoretical results with loss, whereas the red circles give the experimental results. For $\delta = 0$ (Fig. 4a), the transmission coefficient presents a maximum value around $\Omega = 1$, where the BIC is hidden and does not give any signature in the transmission spectrum, the corresponding resonance having a zero width. In this case, the reflection tends to zero and the absorption shows a weak value around 0.1. By slightly shifting from BIC condition (Fig. 4b), the FP-BIC transforms into a quasi-BIC with a Fano shape. Furthermore, one can observe from Figs. 4b–d that the width of the resonance increases and its intensity decreases in the transmission spectra as δ increases. The reflection increases with δ and reaches a maximum value of 0.55, while the absorption presents a maximum value of 0.56 around $\delta_{th} = 20$ cm and decreases for $\delta > 20$ cm. The experimental results (open circles) are in good agreement with the theoretical ones (solid lines) in the presence of loss. It is worth noting that the loss affects considerably the shape of Fano resonances around $\Omega = 1$.

Figure 5 gives the theoretical variation of the transmission (red line), reflection (blue line) and absorption (green line) versus δ at $\Omega = 1$. One can see that the absorption A increases for small values of δ and goes through a maximum $A_{max} \simeq 0.56$ around $\delta_{th} \simeq 20$ cm and then decreases for $\delta > 20$ cm. This behavior happens when the transmission and reflection become equal (i.e., $T = R \simeq 0.22$). These results show that the peak in the absorption can be controlled by detuning the lengths of the two arms.

To characterize better the BICs and Fano resonances, we give in Fig. 6 a comparison between $\Delta n(\omega)$ which is a fundamental physical quantity and the derivative of the Friedel phase which can be measured from the experiment as a function of the dimensionless

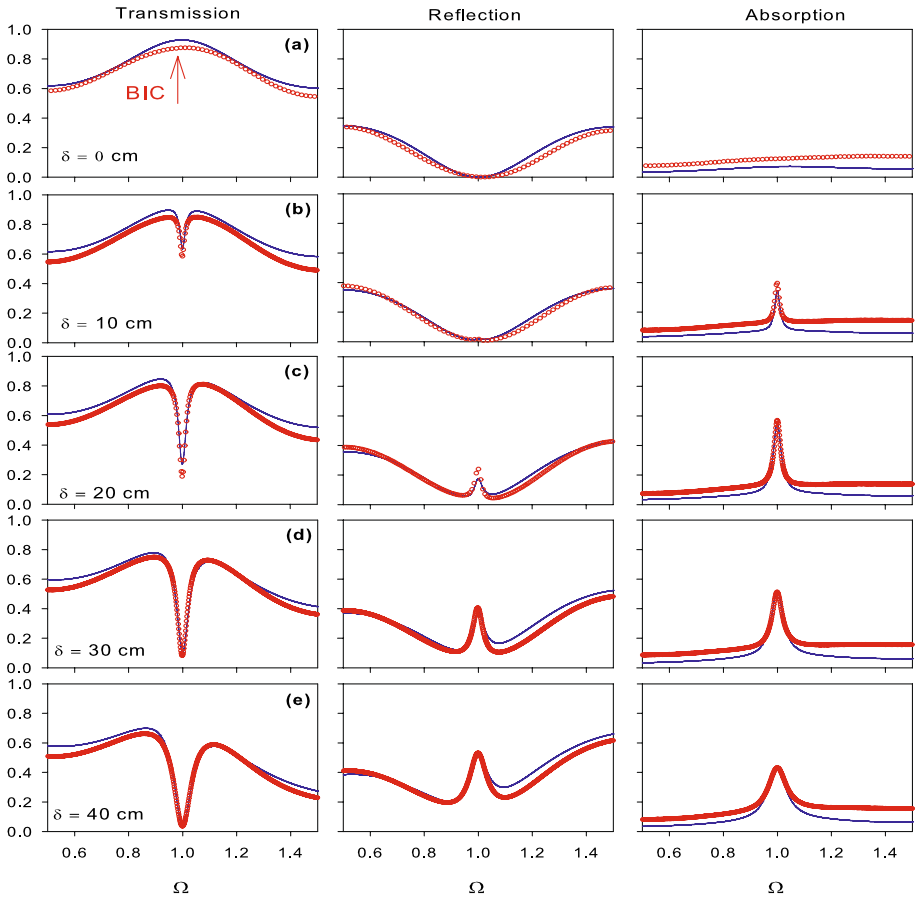

Fig. 4 Transmission, reflection and absorption versus the dimensionless frequency Ω for different values of δ. The blue lines are the theoretical results, whereas the open circles represent experimental data

frequency Ω for different values of δ. The variation of DOS (green lines) is obtained from Eq. (17), while the derivative of the Friedel phase $\frac{d\theta_f}{d\omega}$ (pink dashed lines) is given by Eq. (20). In the absence of loss, One can notice a very good agreement between $2\pi\Delta n(\omega)$ and $\frac{d\theta_f}{d\omega}$ in accordance with Eq. (21) and confirm the results discussed in Sect. 2.3. As mentioned before, BIC appears as delta peak in the DOS with zero width as shown in Fig. 6a. However, the DOS still shows a broad resonance as illustrated in the inset of Fig. 6a. Now, by slightly shifting from the BIC (i.e., $\delta \neq 0$), a classical Breit Weigner resonance appears as a well defined peak characterized by a finite width and a finite intensity. Also, the width of the resonance increases with δ, while its intensity decreases.

As mentioned previously, the relation between the DOS and the derivative of the Friedel phase $\frac{d\theta_f}{d\omega}$ are exact for a lossless system. However, the presence of loss can affect significantly the above relations. Indeed, from Fig. 5, we can expect different behaviors of $det(S)$ around $\delta = \delta_{th}$ where $R = T$. In order to give a better insight about the effect of dissipation on these two quantities, we have plotted in Fig. 7 a comparison between $\Delta n(\omega)$ (green dashed lines) and $\frac{d\theta_f}{d\omega}$ (pink lines) for different values of δ around δ_{th}. For $\delta = 0$, Fig. 7a shows that the BIC

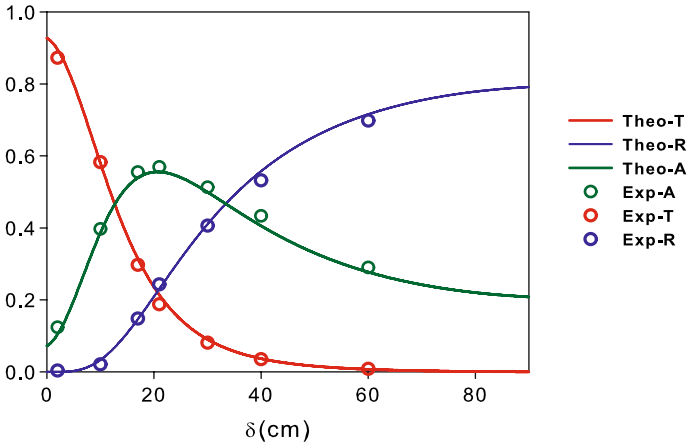

Fig. 5 Theoretical variation of the transmission (red line), reflection (blue line) and absorption (green line) versus δ at the resonance $\Omega = 1$ in Fig. 4. Open circles correspond to experimental data. (Color figure online)

appears as a delta peak in $\Delta n(\omega)$ with an infinite quality factor as indicated by the dashed line. For $\delta \neq 0$, $\Delta n(\omega)$ and $\frac{d\theta_f}{d\omega}$ exhibit different behaviors around $\Omega = 1$ and $\delta = \delta_{th} = 22$ cm as shown in Figs. 7b–e. Indeed, for $\delta = \delta_{th}$ we have found that $det(S)$ vanishes (i.e., $t \simeq \pm r$) at $\Omega = 1$ and its argument becomes ill-defined. However, for $\delta < \delta_{th}$ ($\delta > \delta_{th}$), $Img[det(S)]$ changes sign at $\Omega = 1$, whereas $Re[det(S)]$ remains positif (negative). Therefore, $Arg[det(S)]$ decreases (increases) around $\Omega = 1$ for $\delta < \delta_{th}$ ($\delta > \delta_{th}$) as it is shown in the supplementary material (Figs. S1a, b). However, the variation of the number of states given by $Arg[g(MM)]$ increases monotonically as a function of Ω whatever the value of δ (See Fig. S1 c). Consequently, for $\delta < \delta_{th}$, $\Delta n(\omega)$ is different from $\frac{d\theta_f}{d\omega}$ because of the phase drop of $Arg[det(S)]$ giving rise to a negative enlarged delta peak as shown in Figs. 7b and c for $\delta = 10$ cm and $\delta = 20$ cm respectively. Whereas, for $\delta > \delta_{th}$, $\Delta n(\omega)$ becomes almost similar to $\frac{d\theta_f}{d\omega}$ as shown in Figs. 7d and e for $\delta = 30$ cm and $\delta = 40$ cm respectively.

It is worth noting that the other BICs in Fig. 2 present the same behavior as for the pair $(m = 1, n = 1)$. An example is given in the supplementary material SM2 (Fig. S2) for the pair $(m = 5, n = 3)$. Also, we have checked theoretically and experimentally that the absorption can be accurately derived from $|det(S)|$ (i.e., $A \simeq 1 - |det(S)|$). This result is given in the supplementary material (Fig. S1d) for $\delta = 20$ cm. Finally, let us mention that the threshold value δ_{th} decreases as far as the strength of the attenuation (ϵ'') decreases. However, the results in Fig. 5 remain qualitatively the same and the relationship between DOS and $\frac{d\theta_f}{d\omega}$ remains also valid for $\delta < \delta_{th}$ and $\delta > \delta_{th}$.

4 Analytical and numerical results in the infrared domain

In this section, we give another analytical and numerical application of the results presented in the previous section to plasmonic nano-waveguides operating in the infrared domain. Also, we show the usefulness of the Fano resonances for sensing applications. Therefore, we consider a plasmonic structure composed of a rectangular metal-insulator-metal (MIM) ring resonator inserted between two semi-infinite MIM waveguides

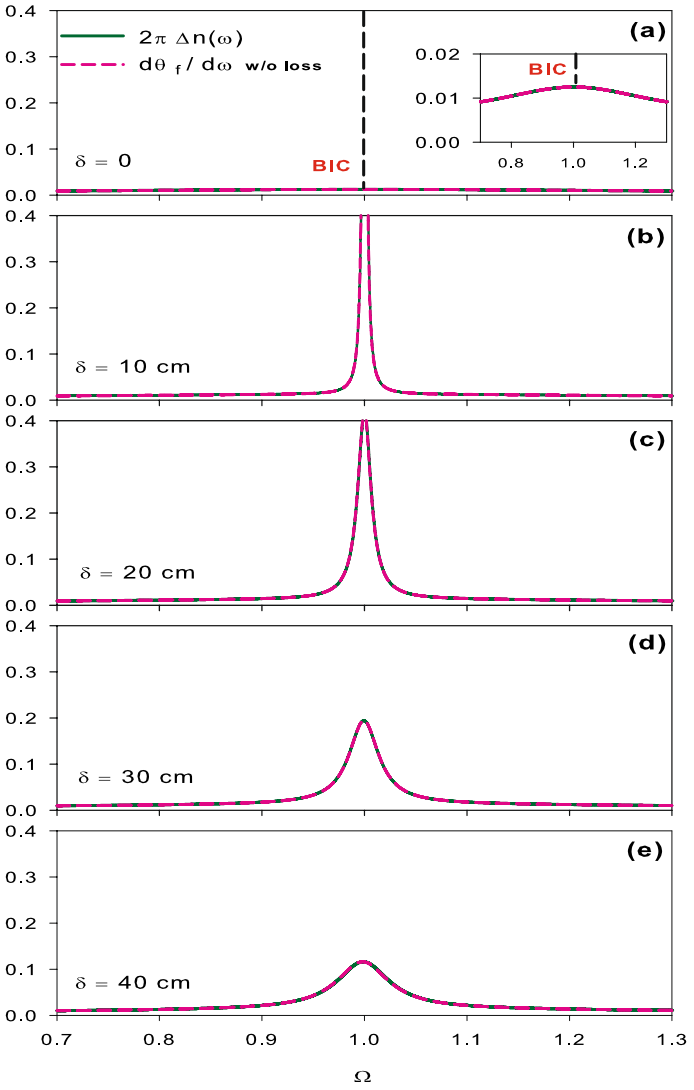

Fig. 6 Theoretical variation of the derivative of the Friedel phase $\frac{d\theta_f}{d\omega}$ (pink dashed line), and the variation of DOS $\Delta n(\omega)$ (green solid lines) for different values of δ in a lossless system. The position of the BIC at $\delta = 0$ is indicated by the vertical dashed line (delta peak) in (a)

(Fig. 1c). The length of the rectangular ring is fixed to $L = d_1 + d_2 = 1400$nm, whereas the detuning between the two arms $\delta = d_2 - d_1$ is chosen variable. The waveguides are filled with air, while the surrounding metal is made of silver with a dielectric constant ε_m given by the Drude model (Maier 2007; Zhang and Wang 2019)

$$\varepsilon_m = \varepsilon_\infty - \frac{\omega_p^2}{\omega^2 + j\gamma\omega}, \tag{24}$$

where $\varepsilon_\infty = 3.7$ is the infinite frequency permittivity, $\gamma = 2.634 \times 10^{13}$ rad/s is the electron collision frequency, $\omega_p = 1.38 \times 10^{16}$ rad/s the bulk plasma frequency of silver, and ω is

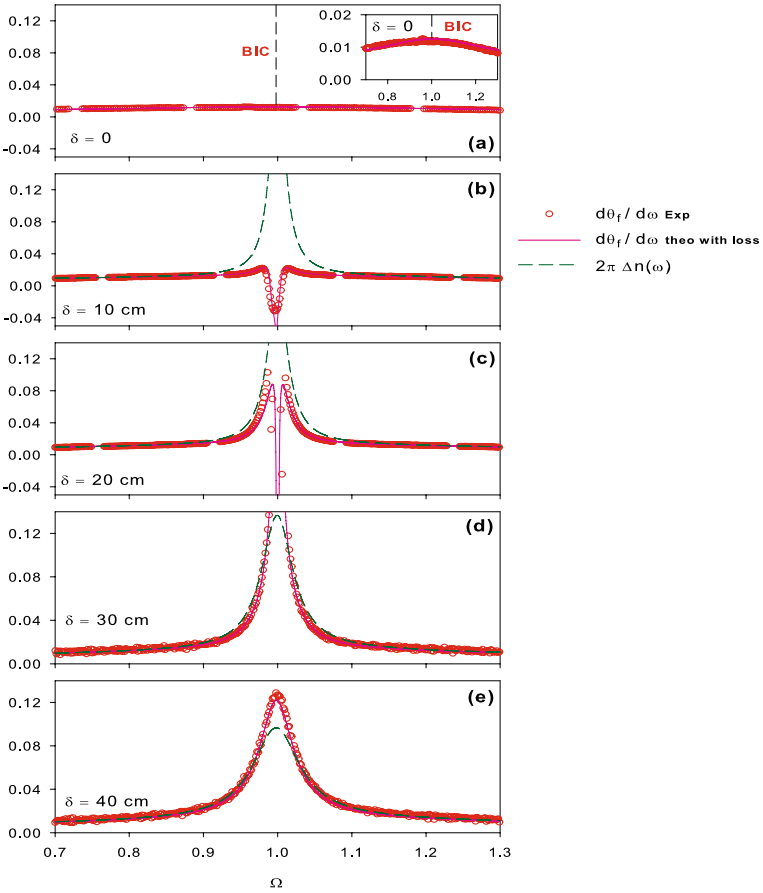

Fig. 7 Same as in Fig. 6 but for a lossy system. The theoretical results of $\frac{d\theta_f}{d\omega}$ (pink solid lines) are validated by the experimental data (red open circles). The variation of DOS ($\Delta n(\omega)$) is plotted with green dashed lines

the angular frequency of the incident light. These parameters are obtained by fitting the experimental data (Han and Bozhevolnyi 2011) at the infrared domain. The width of the MIM waveguide has been chosen to be d=50 nm in order to ensure that only the fundamental transverse magnetic (TM_0) mode is supported.

The plasmonic device presented in Fig. 1c is 2D system in the (x, y) plane and infinite in the z-direction. This design is the most used in MIM waveguides simulations as it is less time consuming. However, for practical processing, the MIM waveguides are 3D as they present a finite height "h" along the z-direction and they are deposited on SiO_2 (or Si) substrate and terminated by air. The finite depth of the system and the surrounding media introduce a significant effect on loss in the system. Nevertheless, it was shown that above a certain height ($h = 50$ nm), 2D and 3D models provide almost similar results in particular as concerns the positions of the resonant modes in the transmission spectra (Niu et al. 2016); however, their shapes and widths are considerably affected. The analytical results of section 2.2 will be compared with numerical simulations based on a two-dimensional (2D)

finite element method used to simulate the transmission spectra through the plasmonic device depicted in Fig. 1c using Comsol Multiphysics software.

First, it is necessary to introduce the surface plasmon polariton (SPP) propagation wavevector k_{sp} and the impedance of the MIM waveguide Z. Here, we focus on the MIM waveguide which only supports the symmetric TM_0 mode and for sufficiently small dielectric thickness d (i.e., d $\ll \lambda_{sp}$), the wavevector k_{sp} can be obtained from a Taylor expansion of the dispersion relation of the MIM system, namely (Maier 2007)

$$k_{sp} = k_0 \sqrt{\varepsilon_d - \frac{2\varepsilon_d \sqrt{\varepsilon_d - \varepsilon_m}}{\varepsilon_m k_0 d}}, \tag{25}$$

where ε_d and ε_m are the dielectric constants of the dielectric and the metal respectively. $k_0 = \frac{\omega}{c}$ is the wave vector in vacuum and c is the speed of light in vacuum.

Another interesting physical quantity in the Green's function method is the impedance Z of the MIM waveguide, this quantity is given by Maier (2007), Zhang and Wang (2019)

$$Z = \frac{k_{sp} d}{\varepsilon_d \omega}. \tag{26}$$

By using Eqs. (25) and (26), the calculation of the transmission coefficient and the dispersion relation as well as DOS are similar to those presented in Sect. 2.2, just we need to replace in Eq. (3), k by k_{sp} (Eq. (25)) and F by ωZ where Z is given by Eq. (26). Let us mention that the definition of the parameter F in the plasmonic system is the inverse of that of the photonic system (Eq. (4)) as the Green's function of the latter is defined from the electric field, while that of the former is defined from the magnetic field.

In order to excite the symmetric guided plasmon (with respect to the symmetry plane in the middle of the MIM-guide) in which we are interested, a boundary mode analysis is set prior to the wave propagation study at the inlet/outlet of the structure. This step solves for the fields and associated propagation constant $k_{sp} \equiv k_x$ which can propagate in the MIM structure. The frequency domain which we are interested in here corresponds to the Infrared (IR) domain ranging from 1200 to 2600 nm. In this frequency interval, the waveguide is strictly mono-mode and antisymmetric (Bah et al. 1992). It corresponds to a SPP-like mode in which the electric field is strongly confined along the dielectric- metal interface and decays exponentially away from it (Noual et al. 2009, 2017). Concerning the employed mesh, we set the mesh maximal step size in the dielectric as $\Delta \leq \lambda_0/6$ (i.e., six elements per wavelength) whilst in the metal at least 5 to 6 points per the silver metal skin depth ~ 20 nm are to be set, so we chose $\Delta \sim 2$ nm to guarantee a good numerical convergence. On the other hand, we take numerically benefit from the ports boundary conditions to compute the transmission/reflection spectra. This comes from the scattering matrix of the structure S (Eq. (18)) which is automatically set whenever ports are used in Comsol.

Similarly to the photonic case, we plot in Figs. 8a and b the analytical and numerical variation of the transmission intensity (in color scale) versus the wavelength and the detuning δ with $L = d_1 + d_2 = 1400$ nm, respectively. Also, in this optical range, we prefer to use the wavelength instead of frequency. Here, we focus on the second BIC corresponding to $(m = 2, n = 2)$ which falls in the near infrared domain. One can see that the BIC falls at $\lambda = 1707$ nm for $\delta = 0$. By detuning δ from the BIC position, the latter transforms to a Fano resonance with a finite width as shown in Fig. 8. These results are qualitatively similar to those found in the photonic loop system (Fig. 2a and the inset in Fig. 3) but in the infrared domain. Also, one can notice that the transmission intensity does not reach unity ($T_{max} = 0.8$)

because of the intrinsic loss in the MIM waveguides. We can see a good agreement between the analytical (Fig. 8a) and numerical (Fig. 8b) results.

To give a better insight about the behavior of BIC in the transmission spectra, we present in Fig. 9 the transmission versus the wavelength for $\delta = 0$ (Fig. 9a) and $\delta = 50$ nm (Fig. 9b). For $\delta = 0$, one can notice the existence of a BIC with zero width around $\lambda_r = 1707$ nm indicated by the black arrow. Now, in order to show the existence of a Fano resonance, we detune slightly δ from $\delta = 0$, this is shown in Fig. 9b for $\delta = 50$ nm. The analytical (open triangles) and numerical (solid lines) results are compared together in Figs. 9a and b revealing a good agreement between them which validate the accuracy of the analytical results. Also, we have checked that the absorption coefficient can reach a maximum value around $A = 0.53$ for $\delta_{th} = 38.5$ nm similarly as in Fig. 5 (see Fig. S3 in the supplementary material SM3).

Plasmonic MIM waveguides coupled side with a ring resonator have been considered as one of the most promising ways for developing nanoscale integrated optical circuits and they are appropriate candidates for refractive index sensing. Indeed, Fano resonance is extremely sensitive to changes in the refractive index in the waveguide (Hayashi et al. 2015), which provides a very promising pathway to achieve a high sensitive sensor efficiency. The sensitivity and the figure of merit (FOM) are the most important factors that characterize the sensor. The sensitivity is determined by the shift of the resonance wavelength $\Delta\lambda$ due to the changes in the refractive index Δn, and is defined as

$$\text{Sensitivity} = \frac{\Delta\lambda}{\Delta n}, \tag{27}$$

whereas, FOM is given by

$$\text{FOM} = \frac{\text{Sensitivity}}{\text{FWHM}}, \tag{28}$$

where FWHM is the full width at half maximum of the resonance dip.

The transmission amplitudes are calculated and simulated using different filling media in the waveguide in order to investigate the effect of the refractive index n on Fano resonance for $\delta = 50$ nm. The analytical (open circles) and numerical results are plotted in Fig. 9c for different refractive index from $n = 1$ to $n = 1.1$ with a step of 0.02, leading to a shift of the spectra when n increases. Figure 9d shows the shift of the Fano resonance

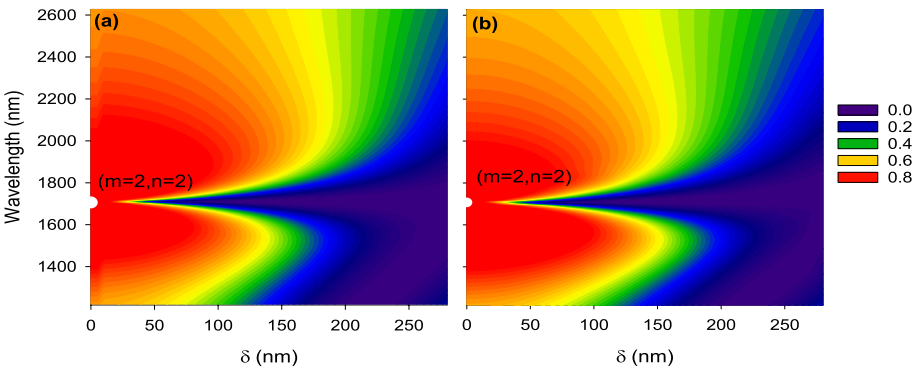

Fig. 8 **a** Analytical and **b** numerical variation of the transmission (with color scale) versus the wavelength and the detuning δ. The white circle indicates the position of the BIC

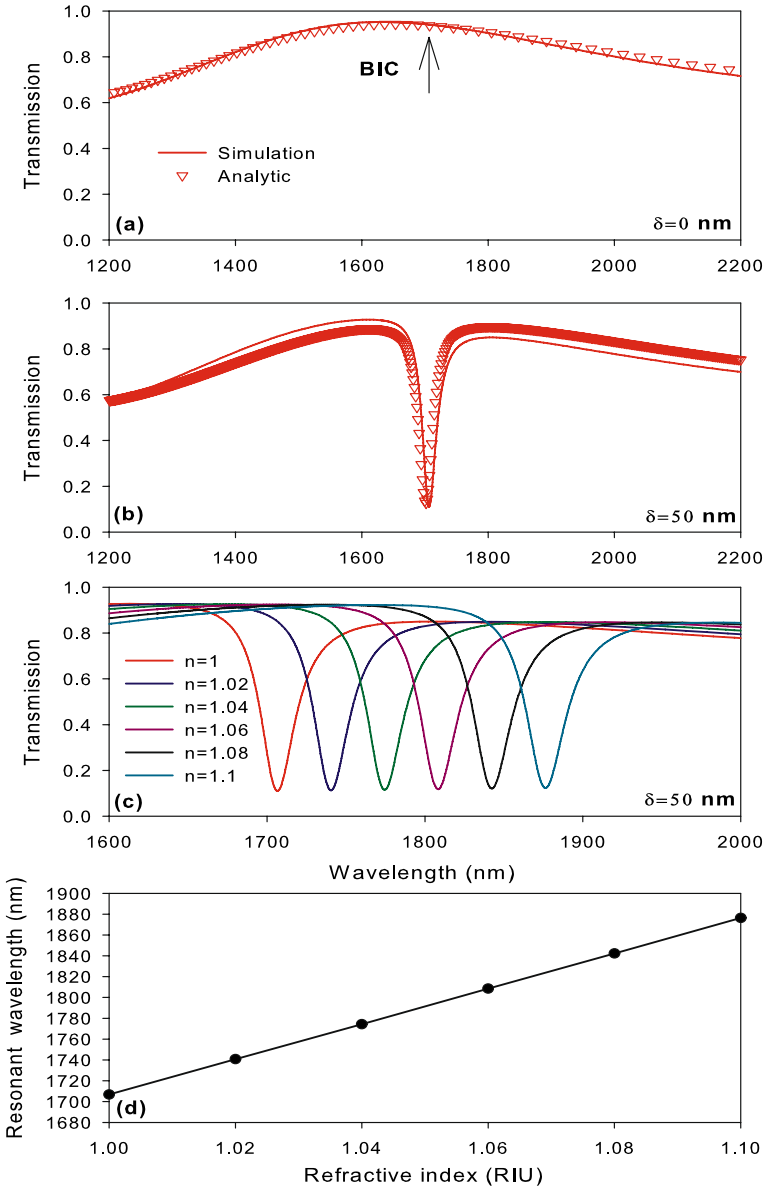

Fig. 9 Transmission spectra versus the wavelength for $\delta = 0$ (**a**) and $\delta = 50$ nm (**b**). **c** Same as (**b**) but for different refractive index n in the waveguide. **d** Resonant wavelength versus the refractive index n of the material filling the waveguide

as a function of n. The fitting between n and the resonance wavelength has a linear relationship from which one can deduce a maximum sensitivity of 1712 nm/RIU and a FOM of 66 RIU^{-1}. Let us mention that the sensitivity and FOM depend on $L = d_1 + d_2$ and the detuning δ and also on the choice of the mode number (m, n). If we take for example $L = 1800$ nm and $\delta = 40$ nm for the first mode (1, 1), we find *Sensitivity* = 2400 nm/RIU

and $FOM = 94$ around $\lambda = 2393$ nm. However, in this case the numerical results do not match sufficiently with the analytical ones. These results are given in the supplementary material SM3 (Figs. S4a and b).

Table 1 gives a comparison of our results on the sensitivity and FOM with those of other plasmonic refractive index sensors based on a MIM waveguide with a side-coupled ring resonator published in the literature. In comparison to other similar sensors studied recently, the proposed design shows very good performances. It is worth noting that the plasmonic sensor can also sense the refractive index change of water and bio-cells and therefore can be used as a biosensor (Zhang et al. 2018). The compact design of the sensor makes it suitable to be integrated into the on-chip optical sensing platforms.

5 Conclusion

In summary, we have given an analytical evidence about the existence of BICs and Fano resonances in a single loop made of two arms of lengths d_1 and d_2 with both an experimental validation in the radio-frequency domain using coaxial cables and a numerical validation in the infrared domain using plasmonic MIM waveguides. The whole system is inserted between two semi-infinite wires. The analytical results obtained with the help of the Green's function method are confirmed by the experimental measurements using the coaxial cables in the radio-frequency regime. We have demonstrated analytically that the loop system may exhibit BICs for particular values of δ such that d_1 and d_2 are commensurate. These modes appear as resonances with zero width in the transmission spectra, as well as in the DOS for lossless system. By slightly shifting δ from that corresponding to BICs, one can obtain Fano resonances with finite width known as quasi-BICs with an anti-resonance shape. Additionally, for a lossy system and depending on the detuning δ between the two arms, the absorption may goes to a maximum value of around 0.56 for a threshold $\delta_{th} = 22$ cm. This behavior occurs when the transmission and reflection become equal ($R = T \simeq 0.22$). Also, we have given a comparative study of DOS and Friedel phase (or equivalently the argument of the determinant of the scattering matrix). In particular, we have shown that for a lossless system, the DOS is proportional to the derivative of the Friedel phase, while for a lossy system, one can distinguish two cases: i) for $\delta < \delta_{th}$, the Friedel phase decreases around certain frequencies giving rise to a negative enlarged delta peak in the derivative of the Friedel phase and the DOS becomes different from the latter. ii) For $\delta > \delta_{th}$, the DOS is equivalent to the derivative of the Friedel phase. Also, we have demonstrated that the absorption coefficient can be extracted from the modulus of $det(S)$ which is

Table 1 Comparison results of the proposed plasmonic rectangular ring with previous works

Structure	Year	Sensitivity (nm/RIU)	FOM
Ref Tang et al. (2017)	2017	1000	63
Ref Zhang et al. (2018)	2018	1700	60.7
Ref Butt et al. (2019)	2019	1367	25
Ref Rahmatiyar et al. (2020)	2020	1295	159.6
Ref Zhu and Wu (2021)	2021	825	21.54
Ref Al Mahmud et al. (2021)	2021	2713	35.1
This work	2021	2400	95

a measurable quantity. Finally, we have given a transposition of these results to plasmonic MIM waveguides operating in the infrared domain by taking properly the lengths of the two arms of the loop at the nanoscale. The last structure is proposed to realize an efficient refractive index sensor. Here also the analytical results (obtained by the Green's function approach) are in good agreement with the numerical results obtained by the finite element method. The results presented in this work can be transposed to acoustic waveguides in the audible frequency domain (Robertson et al. 2007).

Author Contributions M. Amrani, S. Khattou, H. Al-Wahsh and Y. Rezzouk developed the theoretical formalism, performed the analytical calculations and numerical simulations. A. Talbi and C. Ghouila-Houri performed the experiments. E.H. El Boudouti, B. Djafari-Rouhani, A. Akjouj and L. Dobrzynski planned and supervised the work. All authors contributed to the discussion and preparation of the manuscript.

Funding This study was funded by the National Center of Scientific and Technical Research (CNRST), Morocco.

Availability of data and materials The data that support the findings of this study are available from the corresponding author upon reasonable request.

Code availability The codes that support the findings of this study are available from the corresponding author upon reasonable request.

Declarations

Conflict of interest The authors declare no competing interests.

Consent to participate All authors accepted.

Consent for publication All authors accepted.

References

Al Mahmud, R., Faruque, M.O., Sagor, R.H.: A highly sensitive plasmonic refractive index sensor based on triangular resonator. Opt. Commun. **483**, 126634 (2021)

Algorri, J.F., Dell'Olio, F., Roldán-Varona, P., Rodríguez-Cobo, L., López-Higuera, J.M., Sánchez-Pena, J.M., Zografopoulos, D.C.: Strongly resonant silicon slot metasurfaces with symmetry-protected bound states in the continuum. Opt. Express **29**, 10374 (2021)

Al-Wahsh, H., El Boudouti, E.H., Djafari-Rouhani, B., Akjouj, A., Dobrzynski, L.: Transmission gaps and sharp resonant states in the electronic transport through a simple mesoscopic device. Phys. Rev. B **75**, 125313 (2007)

Amrani, M., Quotane, I., Ghouila-Houri, C., El Boudouti, E.H., Krutyansky, L., Piwakowski, B., Pernod, P., Talbi, A., Djafari-Rouhani, B.: Experimental evidence of the existence of bound states in the Continuum and Fano resonances in solid-liquid layered media. Phys. Rev. Appl. **15**, 054046 (2021)

Azzam, S.I., Shalaev, V.M., Boltasseva, A., Kildishev, A.V.: Formation of bound states in the continuum in hybrid plasmonic-photonic systems. Phys. Rev. Lett. **121**, 253901 (2018)

Bah, M.L., Akjouj, A., Dobrzynski, L.: Response functions in layered dielectric media. Surf. Sci. Rep. **16**, 95–132 (1992)

Bogdanov, A.A., Koshelev, K.L., Kapitanova, P.V., Rybin, M.V., Gladyshev, A.S., Sadrieva, Z.F., Samusev, K.B., Kivshar, Y.S., Limonov, M.F.: Bound states in the continuum and Fano resonances in the strong mode coupling regime. Adv. Photonics **1**, 06001 (2019)

Bulgakov, E.N., Pichugin, K.N., Sadreev, A.F., Rotter, I.: Bound states in the continuum in open Aharonov-Bohm rings. JETP Lett. **84**, 430–435 (2006)

Büttiker, M.: Capacitance, admittance, and rectification properties of small conductors. J. Phys.: Condens. Matter **5**, 9361 (1993)
Butt, M.A., Khonina, S.N., Kazanskiy, N.L.: Plasmonic refractive index sensor based on metal-insulator-metal waveguides with high sensitivity. J. Mod. Opt. **66**, 1038–1043 (2019)
Chen, J., Li, J., Liu, X., Rohimah, S., Tian, H., Qi, D.: Fano resonance in a MIM waveguide with double symmetric rectangular stubs and its sensing characteristics. Opt. Commun. **482**, 126563 (2021)
Chou Chao, C.-T., Chou Chau, Y.-F., Chiang, H.-P.: Multiple Fano resonance modes in an ultra-compact plasmonic waveguide-cavity system for sensing applications. Res. Phys. **27**, 104527 (2021)
Conteduca, D., Barth, I., Pitruzzello, G., Reardon, C.P., Martins, E.R., Krauss, T.F.: Dielectric nanohole array metasurface for high-resolution nearfeld sensing and imaging. Nat. commun. **12**, 3293 (2021)
Cui, X., Tian, H., Du, Y., Shi, G., Zhou, Z.: Normal incidence filters using symmetry-protected modes in dielectric subwavelength gratings. Sci. Rep. **6**, 36066 (2016)
Dobrzynski, L., Akjouj, A., El Boudouti, E.H., Lévêque, G., Al-Wahsh, H., Pennec, Y., Ghouila-Houri, C., Talbi, A., Djafari-Rouhani, B., Jin, Y.: Photonics. Elsevier (2020)
Doskolovich, L.L., Bezus, E.A., Bykov, D.A.: Integrated flat-top reflection filters operating near bound states in the continuum. Photonics Res. **7**, 1314–1322 (2019)
El Boudouti, E.H., Fettouhi, N., Akjouj, A., Djafari-Rouhani, B., Mir, A., Vasseur, J.O., Dobrzynski, L., Zemmouri, J.: Experimental and theoretical evidence for the existence of photonic bandgaps and selective transmissions in serial loop structures. J. Appl. Phys. **95**, 1102–1113 (2004)
Fano, U.: Effects of configuration interaction on intensities and phase shifts. Phys. Rev. **124**, 1866 (1961)
Friedel, J.: The distribution of electrons around impurities in monovalent metals. Philos. Mag. **43**, 153–189 (1952)
Hajshahvaladi, L., Kaatuzian, H., Danaie, M., Karimi, Y.: Design of a highly sensitive tunable plasmonic refractive index sensor based on a ring-shaped nano-resonator. Opt. Quantum Electron. **54**, 1–17 (2022)
Han, Z., Bozhevolnyi, S.I.: Plasmon-induced transparency with detuned ultracompact Fabry-Perot resonators in integrated plasmonic devices. Opt. Express **19**, 3251–3257 (2011)
Hayashi, S., Nesterenko, D.V., Sekkat, Z.: Waveguide-coupled surface plasmon resonance sensor structures: Fano lineshape engineering for ultrahigh-resolution sensing. J. Phys. D: Appl. Phys. **48**, 325303 (2015)
Ha, S.T., Fu, Y.H., Emani, N.K., Pan, Z., Bakker, R.M., Paniagua-Domínguez, R., Kuznetsov, A.I.: Directional lasing in resonant semiconductor nanoantenna arrays. Nat. Nanotechnol **13**, 1042–1047 (2018)
He, F., Liu, J., Pan, G., Shu, F., Jing, X., Hong, Z.: Analogue of electromagnetically induced transparency in an all-dielectric double-layer metasurface based on bound states in the continuum. Nanomaterials **11**, 2343 (2021)
Hsueh, W.-J., Qiu, R.-Z., Chen, C.-H.: Resonant transport and giant persistent currents in double-asymmetric rings. Eur. Phys. J. B **86**, 27 (2013)
Hsu, C.W., Zhen, B., Stone, A.D., Joannopoulos, J.D., Soljačić, M.: Bound states in the continuum. Nat. Rev. Mater. **1**, 16048 (2016)
Huang, L., Chiang, Y.K., Huang, S., Shen, C., Deng, F., Cheng, Y., Jia, B., Li, Y., Powell, D.A., Miroshnichenko, A.E.: Sound trapping in an open resonator. Nat. Commun. **12**, 4819 (2021)
Khattou, S., Amrani, M., Mouadili, A., El Boudouti, E.H., Talbi, A., Akjouj, A., Djafari-Rouhani, B.: Comparison of density of states and scattering parameters in coaxial photonic crystals: theory and experiment. Phys. Rev. B **102**, 165310 (2020)
Kobayashi, K., Aikawa, H., Sano, A., Katsumoto, S., Iye, Y.: Fano resonance in a quantum wire with a side-coupled quantum dot. Phys. Rev. B **70**, 035319 (2004)
Lee, H.-W.: Generic transmission zeros and in-phase resonances in time-reversal symmetric single channel transport. Phys. Rev. Lett. **82**, 2358 (1999)
Limonov, M.F., Rybin, M.V., Poddubny, A.N., Kivshar, Y.S.: Fano resonances in photonics. Nat. Photonics **11**, 543–554 (2017)
Liu, X., Yang, Q., Peng, K., Zhang, B., Bai, H., Li, X., Tan, Y., Zhang, Z., Guo, F.: Tunable triple Fano resonance in MIM waveguide system with split ring resonator. Opt. Quantum Electron. **53**, 1–12 (2021)
Maier, S.A.: Plasmonics: Fundamentals and Applications. Springer (2007)
Miroshnichenko, A.E., Flach, S., Kivshar, Y.S.: Fano resonances in nanoscale structures. Rev. Mod. Phys. **82**, 2257 (2010)
Mrabti, T., Labdouti, Z., El Abouti, O., El Boudouti, E.H., Fethi, F., Djafari-Rouhani, B.: Transmission gaps, trapped modes and Fano resonances in Aharonov Bohm connected mesoscopic loops. Phys. Lett. A **382**, 613–620 (2018)
Mrabti, T., Labdouti, Z., Mouadili, A., El Boudouti, E.H., Djafari-Rouhani, B.: Aharonov-Bohm-effect induced transparency and reflection in mesoscopic rings side coupled to a quantum wire. Physica E **116**, 113770 (2020)

Niu, L., Xiang, Y., Luo, W., Cai, W., Qi, J., Zhang, X., Xu, J.: Nanofocusing of the free-space optical energy with plasmonic Tamm states. Sci. Rep. **6**, 39125 (2016)
Noual, A., Pennec, Y., Akjouj, A., Djafari-Rouhani, B., Dobrzynski, L.: Nanoscale plasmon waveguide including cavity resonator. J. Phys.: Condens. Matter **21**, 375301 (2009)
Noual, A., El Abouti, O., El Boudouti, E.H., Akjouj, A., Pennec, Y., Djafari-Rouhani, B.: Plasmonic-induced transparency in a MIM waveguide with two side-coupled cavities. Appl. Phys. A **123**, 49 (2017)
Pankin, P.S., Wu, B.R., Yang, J.H., Chen, K.P., Timofeev, I.V., Sadreev, A.F.: One-dimensional photonic bound states in the continuum. Commun. Phys. **3**, 91 (2020)
Qi, Z., Hu, G., Liu, B., Li, Y., Deng, C., Zheng, P., Wang, F., Zhao, L., Cui, Y.: Plasmonic nanocavity for obtaining bound state in the continuum in silicon waveguides. Opt. Express **29**, 9312–9323 (2021)
Quotane, I., El Boudouti, E.H., Djafari-Rouhani, B.: Trapped-mode-induced Fano resonance and acoustical transparency in a one-dimensional solid-fluid phononic crystal. Phys. Rev. B **97**, 024304 (2018)
Rahmatiyar, M., Afsahi, M., Danaie, M.: Design of a refractive index plasmonic sensor based on a ring resonator coupled to a MIM waveguide containing tapered defects. Plasmonics **15**, 2169–2176 (2020)
Rakhshani, M.R.: Fano resonances based on plasmonic square resonator with high figure of merits and its application in glucose concentrations sensing. Opt. Quantum Electron. **51**, 1–16 (2019)
Robertson, W.M., Pappafotis, J., Flannigan, P.: Sound beyond the speed of light: measurement of negative group velocity in an acoustic loop filter. Appl. Phys. Lett. **90**, 014102 (2007)
Sadreev, A.F.: Interference traps waves in an open system: bound states in the continuum. Rep. Prog. Phys. **84**, 055901 (2021)
Sánchez-Meroño, A., Sánchez-López, M.M., Arias, J.: Fast light in unbalanced low-loss Mach-Zehnder interferometers. Phys. Rev. A **89**, 43828 (2014)
Sun, S., Ding, Y., Li, H., Hu, P., Cheng, C.-W., Sang, Y., Cao, F., Hu, Y., Alù, A., Liu, D., Wang, Z., Gwo, S., Han, D., Shi, J.: Tunable plasmonic bound states in the continuum in the visible range. Phys. Rev. B **103**, 045416 (2021)
Tang, Y., Zhang, Z., Wang, R., Hai, Z., Xue, C., Zhang, W., Yan, S.: Refractive index sensor based on fano resonances in metal-insulator-metal waveguides coupled with resonators. Sensors **17**, 784 (2017)
Von Neumann, J., Wigner, E.P.: Uber merkwiirdige diskrete Eigenwerte. Phys. Z. **30**, 465 (1929)
Voo, K.K., Chu, C.S.: Fano resonance in transport through a mesoscopic two-lead ring. Phys. Rev. B **72**, 165307 (2005)
Wu, S., Li, N., Jin, G., Ma, Y.Q.: Persistent current and transmission probability in the Aharonov Bohm ring with an embedded quantum dot. Phys. Lett. A **372**, 2326–2331 (2008)
Wu, F., Wu, J., Guo, Z., Jiang, H., Sun, Y., Li, Y., Ren, J., Chen, H.: Giant enhancement of the Goos-Hänchen shift assisted by quasibound states in the continuum. Phys. Rev. Appl. **12**, 014028 (2019)
Xie, S., Xie, S., Zhan, J., Xie, C., Tian, G., Li, Z., Liu, Q.: Bound states in the continuum in a T-shape nanohole array perforated in a photonic crystal slab. Plasmonics **15**, 1261–1271 (2020)
Xiong, Y.-J., Liang, X.-T.: Fano resonance and persistent current of a quantum ring. Phys. Lett. A **330**, 307–312 (2004)
Zhang, M., Wang, Z.: Analytical method for metal-insulator-metal surface plasmon polaritons waveguide networks. Opt. Express **27**, 303–321 (2019)
Zhang, Z., Yang, J., He, X., Zhang, J., Huang, J., Chen, D., Han, Y.: Plasmonic refractive index sensor with high figure of merit based on concentric-rings resonator. Sensors **18**, 116 (2018)
Zhao, X., Chen, C., Kaj, K., Hammock, I., Huang, Y., Averitt, R.D., Zhang, X.: Terahertz investigation of bound states in the continuum of metallic metasurfaces. Optica **7**, 1548 (2020)
Zhu, J., Wu, C.: Optical refractive index sensor with Fano resonance based on original MIM waveguide structure. Results Phys. **21**, 103858 (2021)
Zou, Z., Liu, J., Zhang, L., Wang, Z., Zhan, L.: Temporal manipulation of light propagation via cross-intensity modulation in unbalanced fiber Mach-Zehnder interferometers. Opt. Express **23**, 29584–29591 (2015)